Journal of Colloid and Interface Science 518 (2018) 156–164

Contents lists available at ScienceDirect

Journal of Colloid and Interface Science

journal homepage: www.elsevier.com/locate/jcis

Regular Article

Regionalized and vectorial charges transferring of $Cd_{1-x}Zn_xS$ twin nanocrystal homojunctions for visible-light driven photocatalytic applications

Wanyue Dong [a,b], Yutang Liu [a,b,*], Guangming Zeng [a,b,*], Shuqu Zhang [c], Tao Cai [a,b], Jili Yuan [c], Hui Chen [a,b], Jing Gao [c], Chengbin Liu [c]

[a] College of Environmental Science and Engineering, Hunan University, Lushan South Road, Yuelu District, Changsha 410082, PR China
[b] Key Laboratory of Environmental Biology and Pollution Control (Hunan University), Ministry of Education, Lushan South Road, Yuelu District, Changsha 410082, PR China
[c] State Key Laboratory of Chemo/Biosensing and Chemometrics, Hunan University, Lushan South Road, Yuelu District, Changsha 410082, PR China

GRAPHICAL ABSTRACT

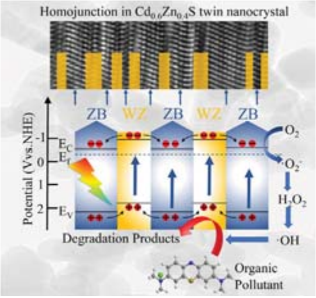

ARTICLE INFO

Article history:
Received 21 November 2017
Revised 1 February 2018
Accepted 6 February 2018
Available online 9 February 2018

Keywords:
Photocatalysis
$Cd_{1-x}Zn_xS$ solid solution
Homojunction
Degradation mechanism

ABSTRACT

In photocatalyst designing, quick recombination of photo-generated electron-hole pairs in the bulk or on the surface of semiconductors is a major limiting factor in achieving high photocatalytic efficiency, which is one of the most knotty scientific issues. For this purpose, a series of $Cd_{1-x}Zn_xS$ twin nanocrystal (NC) zinc blende/wurtzite (ZB/WZ) homojunctions photocatalysts were synthesized by a facile solvothermal route and innovatively employed in photocatalytic degradation. In sample $Cd_{0.6}Zn_{0.4}S$, ZB and WZ phases have the largest distribution and closest interconnection at atomic level. The type-II staggered band alignment formed between two phases made photo-generated electrons and holes spatially separated to ZB (away from twin plane) and WZ (to twin plane) regions, and the ordered arrangement of redox reaction's active sites was then realized inside a single semiconductor. Finally, photocatalytic activities of the samples were evaluated by degradation of methylene blue (MB) upon visible light irradiation. The optimal $Cd_{0.6}Zn_{0.4}S$ NCs without any co-catalyst loading showed high photocatalytic activity with degradation efficiency of 95% in 80 min and performed excellent photostability. Furthermore, photocatalytic degradation and electron transfer mechanisms in $Cd_{0.6}Zn_{0.4}S$ twin NCs are studied particularly. Inner twin structure homojunction has provided a new insight into the crystalline phase engineering.

---

* Corresponding authors at: College of Environmental Science and Engineering, Hunan University, Lushan South Road, Yuelu District, Changsha 410082, PR China.
E-mail addresses: yt_liu@hnu.edu.cn (Y. Liu), zgming@hnu.edu.cn (G. Zeng).

https://doi.org/10.1016/j.jcis.2018.02.018
0021-9797/© 2018 Published by Elsevier Inc.

1. Introduction

In the past few decades, the crisis of environmental pollution and energy shortage have attracted considerable research with respect to solar energy utilization [1–6]. As a green and promising technology, photocatalytic reduction and oxidation reactions, based largely on semiconductors and solar energy, have recently attracted extensive interest in the fields of energy, materials, environment and chemistry [7–13]. Photocatalytic reaction over semiconductors is usually considered as the direct absorption of a photon by the energy band gap of materials [11]. Upon photon excitation, the separated electron and hole can migrate to the semiconductor surface of the catalyst, resulting, for instance, in the degradation of pollutants, the reduction of CO_2 and O_2, the evolution of H_2 and O_2, or the formation of organic compounds. From thermodynamic viewpoint, when the reduction and oxidation potentials lie between the conduction band (CB) and the valence band (VB) potentials, surface reduction and oxidation reactions can be driven by the photo-generated electrons and holes, respectively [14–16]. Therefore, at the most basic level, enhancing charge separation and preventing their recombination before they move to the surface-reactive sites of the photocatalyst plays a key role in determining the solar energy conversion efficiency [17].

To this end, many strategies have been investigated, such as chemical doping to tune the band gap of a photocatalyst [18], surface modification of photocatalysts with co-catalysts, and developing artificial Z-scheme systems [19]. These approaches are coupled with two different materials or phases at the nanoscale to form heterojunctions, which improved interfacial charge transfer, thereby effective charge separation [20–23]. However, these methods have merely considered morphological design and band matching roughly. The designed semiconductor materials fail to obtain precisely tailored-band structures and favorable structure stability.

Phase engineering is a novel strategy, realizing spatial charge separation through internally tuning coordination type. Liu et al. introduced nano-twin structure into $Cd_{1-x}Zn_xS$ photocatalyst without loading noble metal by a one pot hydrothermal method for the first time, and these as-prepared samples exhibited excellent photocatalytic activity for H_2 evolution. Particularly, the twin crystal $Cd_{0.5}Zn_{0.5}S$ solid solution was the most efficient pristine sulphide catalyst ever reported so far for hydrogen production from water without the help of any co-catalyst. In twin crystal structure, the homojunctions were formed between the zinc-blende (ZB) and wurtzite (WZ) segments. Keeping the transport property of free charges as in perfect crystals, the homojunctions can enhance the separation of photo-generated electrons and holes, simultaneously facilitate their transport pathway, and further preventing the recombination of them [17,24].

In this study, we report a series of $Cd_{1-x}Zn_xS$ twin nanocrystal (NC) photocatalysts with tunable band structure synthesized by a facile biomolecule-assisted solvothermal route. Further investigations reveal that the type-II staggered band alignment formed between the ZB and WZ segments would favor the vectorial transfer of photo-induced charges and sequentially distribute the active sites of oxidation reactions and reduction reactions. The highest degradation efficiency (95%) was obtained by the sample $Cd_{0.6}Zn_{0.4}S$. These findings have offered a new idea for the design of novel efficient solar energy-driven semiconductor material for photocatalytic redox reactions through the technique of phase engineering.

2. Experimental

2.1. Chemicals

$Cd(CH_3COO)_2 \cdot 2H_2O$(>99%), $Zn(CH_3COO)_2 \cdot 2H_2O$(>99%), l-cysteine(>99%), diethylenetriamine(DETA) (>98%) were purchased from Sinopharm Chemical Reagent Co., Ltd (Shanghai, China).

2.2. Photocatalyst synthesis

The optimal $Cd_{0.6}Zn_{0.4}S$ (nominal molar ratio of Cd/Zn = 0.6/0.4) NCs were prepared as follows: 3.6 mmol of $Cd(CH_3COO)_2 \cdot 2H_2O$ and 2.4 mmol of $Zn(CH_3COO)_2 \cdot 2H_2O$ were dissolved into 15 mL 58% DETA solution (mixed solvent composed of 6.25 mL distilled water and 8.75 mL of pure DETA). After being stirred for 5 min, 25 mmol of l-cysteine was mixed into the above solution. The mixture solution was further stirred for 30 min to form stable l-cysteine-Cd^{2+}/Zn^{2+}complexes. Then, the mixture was transferred into a Teflon autoclave and heated to 160 °C for 24 h. The product was cooled to room temperature naturally and then centrifuged and washed with double-distilled water and ethanol three times. The obtained product was dried at 60 °C for 12 h in a vacuum oven. Other $Cd_{1-x}Zn_xS$ NCs with different nominal Cd/Zn molar ratios (the total molar amount was kept to be 6 mmol) were synthesized under the same conditions to study the influence of the composition and concentration of DETA and l-cysteine on photocatalytic performance. All the $Cd_{1-x}Zn_xS$ NCs stoichiometry was shown in Table S1. The flowchart of the preparation of $Cd_{1-x}Zn_xS$ NCs are shown in Fig. S1.

2.3. Characterization

The crystal structures characterization of as-prepared samples were determined by X-ray diffraction (XRD) with Cu-Kα radiation (Rigaku, Smartlab). Crystal chemical composition was determined by X-ray photoelectron spectroscopy (XPS) with Al-Kα radiation (Thermo Fisher Scientific, England), the binding energy was calibrated by taking the C 1s peak at 284.8 eV as reference, using Advantage as fitting analysis software, fitting parameters is 100%. The morphologies were determined by field emission scanning electron microscopy (FE-SEM) (Hitachi, S-4800) and transmittance electron microscopy (TEM) (JEOL, JEM-2100F). UV–vis diffuse-reflectance spectra (DRS) were recorded within the 300–800 nm wavelength range using UV–vis spectrophotometer (Cary300, Varian). Electron spin resonance (ESR) spectra were obtained on a JES FA200 electron paramagnetic resonance spectrometer. Electrochemical measurements were performed in mixture of 0.1 M Na_2SO_3 and 0.1 M Na_2S electrolyte solution in a typical three-electrode system that consisted of a working electrode, a platinum wire counter electrode and a saturated calomel reference electrode. The as-prepared photocatalysts thin film on fluorine-doped tin oxide (FTO) was used as the working electrode, the density of photocatalysts is 0.28 mg/cm^2. The electrochemical response was recorded with a CHI 660C electro-chemical analyzer (CHI Inc., USA). The BET specific surface areas were measured on Belsorp-Mini II analyser (Japan).

2.4. Photocatalytic activity measurement

Photocatalytic degradation of MB was conducted vertically irradiated by a 300 W xenon lamp (Beijing China Education Au-light Co. Ltd) with a cutoff filter (≥420 nm). Typically, 20 mg powdered catalysts were dispersed in 50 mL of 10 mg/L MB solution. Then, the solution was magnetically stirred for 30 min in darkness to attain adsorption equilibrium. Aliquots were drawn out of the solution at defined time intervals, centrifuged, and the concentration of reactant remained in supernatants was analyzed by UV–vis spectrophotometer. The initial concentration (C_0) of MB is 10 mg/L. Five successive cyclic tests were implemented over the optimal hybrid as follows. After every run, the sample was washed several times with deionized water, dried at 60°Cin air and subjected to the next run. The degradation efficiency could be calculated as follows:

$$\text{Degradation efficiency}(\%) = \left(1 - \frac{C_t}{C_0}\right) \times 100\%$$

3. Result and discussion

3.1. Morphology and structure characterization

$Cd_{1-x}Zn_xS$ NCs with different nominal x values were prepared by a solvothermal route. X-ray diffraction (XRD) patterns of $Cd_{1-x}Zn_xS$ solid solution NCs are displayed in Fig. 1. XRD patterns of $Cd_{1-x}Zn_xS$ show that the diffraction peaks gradually shift to a high angle with an increase in x value, indicating a decrease in lattice spacing for $Cd_{1-x}Zn_xS$ NCs. The widen diffraction peaks were obtained from the decrease crystal size of $Cd_{1-x}Zn_xS$ NCs. The average crystallite size of $Cd_{1-x}Zn_xS$ NCs calculated by the Scherrer formula Eq (1), with measured mean length and mean width were shown in Table S2.

$$D = K\lambda/(\beta\cos\theta) \tag{1}$$

where D is the particle size, K is the Scherrer constant (0.89), λ is X ray wavelength (0.154056 nm), β is the full width at half maximum of diffraction peak, and θ is the diffraction angle.

In addition, the successive peak shifts imply that the obtained samples are not mixtures of ZnS and CdS but rather $Cd_{1-x}Zn_xS$ solid solutions, which is due to not only the fact that Zn^{2+} cations are incorporated in CdS lattices or its interstitial sites with a smaller ionic radius (Zn^{2+}: 0.74 Å, Cd^{2+}: 0.97 Å) but also that the electronegativity of Zn^{2+} (1.65) is approximately equal to that of Cd^{2+} (1.70) [25].

Usually, photocatalysts with higher specific surface areas are beneficial for the enhancement of photocatalytic performance [26]. Thus, the BET surface areas (S_{BET}) and pore structure of the as-prepared $Cd_{1-x}Zn_xS$ samples were investigated by the nitrogen adsorption-desorption measurement, Fig. S2 shows the nitrogen adsorption/desorption isotherms and the corresponding pore-size distribution curves (inset) of them. According to the Brunauer-Deming-Deming-Teller classification, the isotherms of all the samples are of type IV, indicating the presence of mesopores (2–50 nm) [27–29]. Moreover the isotherms show high adsorption at a high relative pressure (P/P_0) range from 0.8 to 1.0, suggesting the formation of large mesopores and macropores. The pore size distribution curves (insets of Fig. S2) show a wide range further confirming the coexistence of mesopores and macropores [28]. Table S3 shows the quantitative details on the S_{BET} and average pore sizes of the $Cd_{1-x}Zn_xS$ (x = 0, 0.2, 0.4, 0.6, 0.8 and 1.0) samples. The $Cd_{1-x}Zn_xS$ samples show an increasing specific surface areas and decreasing average pore sizes with increasing Zn content. The decreased specific surface areas can be attributed to the increase in the sample density [30]. The increasing pore size is possibly from the formation of larger aggregated particles.

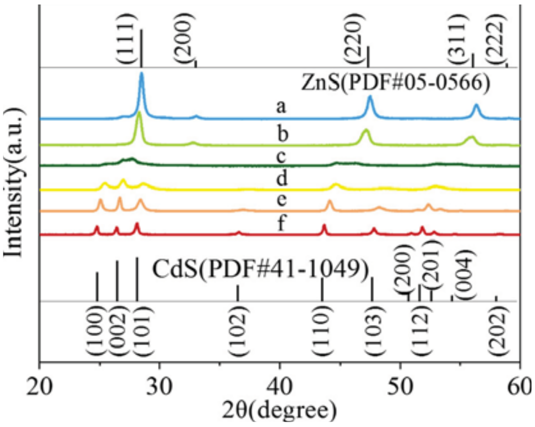

Fig. 1. XRD patterns of $Cd_{1-x}Zn_xS$ solid solution with different x values: (a) 1, (b) 0.8, (c) 0.6, (d) 0.4, (e) 0.2, and (f) 0. The vertical lines at the top and bottom indicate ZnS zinc blende structure (PDF #05-0566) and CdS wurtzite structure (PDF #41-1049).

The SEM images (Fig. S3) have clearly reveals that the overall morphology of $Cd_{0.6}Zn_{0.4}S$ is elongated NCs with an average diameter of around 60 nm, and the morphology of pure ZB ZnS and WZ CdS were also depicted. The TEM and HRTEM images shown in Fig. 2a and b clearly present the anisotropic geometry of the as-prepared sample. It can be seen that $Cd_{0.6}Zn_{0.4}S$ NCs are composed of a high-density parallel distributed stacking faults (see inset in Fig. 2a). The fringes with a lattice spacing of d = 0.34 nm are close to the lattice spacing of the planes of the ZB phase (Fig. 2b). The HRTEM image exhibits that each nanoparticle has a regular strip-like structure, and the particle surface is not as smooth as that found in the SEM image. Nanorod-like NCs are composed of non-uniform zigzag structures. This is due to the fact that ZB/WZ boundaries suddenly destroy the lattice continuity, leading to dislocations residing in coherent twinned boundaries. Fig. 2c shows the Fast Fourier Transformation (FFT) pattern of the $Cd_{0.6}Zn_{0.4}S$ sample, ordered spots appear at the sites one-third from the normal spots known as the diffraction of coherent twins [31,32]. The strips existing on the surface of each NC contain a high density of grown twins of the {1 1 1}/[1 1 2] type. It is suspect that the ZB (zinc blende) segments can be formed by ZnS and the WZ (wurtzite) segments by CdS in the alkaline condition provided by DETA. In sample $Cd_{0.6}Zn_{0.4}S$, due to the proximal contents of Cd and Zn, ZB and WZ are more likely to form regular homojunctions along the ⟨1 1 1⟩ direction [33]. A schematic that illustrate the homojunctions' formation was shown in Fig. 2d. These homojunctions are believed to favor the vectorial transfer of photo-induced charges, which has been extensively explored by heterojunction design [23,34–36].

Scanning TEM (STEM) images (Fig. 3a), elemental mapping (Fig. 3b–d), and energy dispersive X-ray spectrometry (EDX) (Fig. 3e) analysis prove that $Cd_{1-x}Zn_xS$ NCs are homogeneously composed of Zn, Cd, and S elements; these results provide clear evidence for the formation of $Cd_{0.6}Zn_{0.4}S$ solid solutions and preclude the possibility of phase separation between CdS and ZnS, in agreement with XRD results.

X-ray photoelectron spectroscopy (XPS) was carried out to determine the surface chemical compositions and electronic states of $Cd_{0.6}Zn_{0.4}S$ sample (Fig. 4). The XPS survey spectrum reveals the existence of Zn, Cd, and S elements (Fig. 4a), indicating the successful synthesis of solid solution. The sharp peaks located at 1021.24 and 1044.49 eV as shown in Fig. 4b can be assigned to the Zn $2p_{3/2}$ and Zn $2p_{1/2}$ levels, respectively. The peaks of Cd $3d_{5/2}$ and Cd $3d_{3/2}$ are found at 404.59 and 411.34 eV in Fig. 4c. The peaks of Zn $2p_{3/2}$, Zn $2p_{1/2}$, Cd $3d_{5/2}$ and Cd $3d_{3/2}$ are all sharp and symmetrical, demonstrating that the valences of Zn and Cd in the samples are both + 2 [37,38]. In the S 2p region, the band can be deconvoluted into two peaks (161.04 eV and 162.24 eV), which can be attributed to the S $2p_{3/2}$ and S 2p1/2 levels, respectively [39]. Based on the

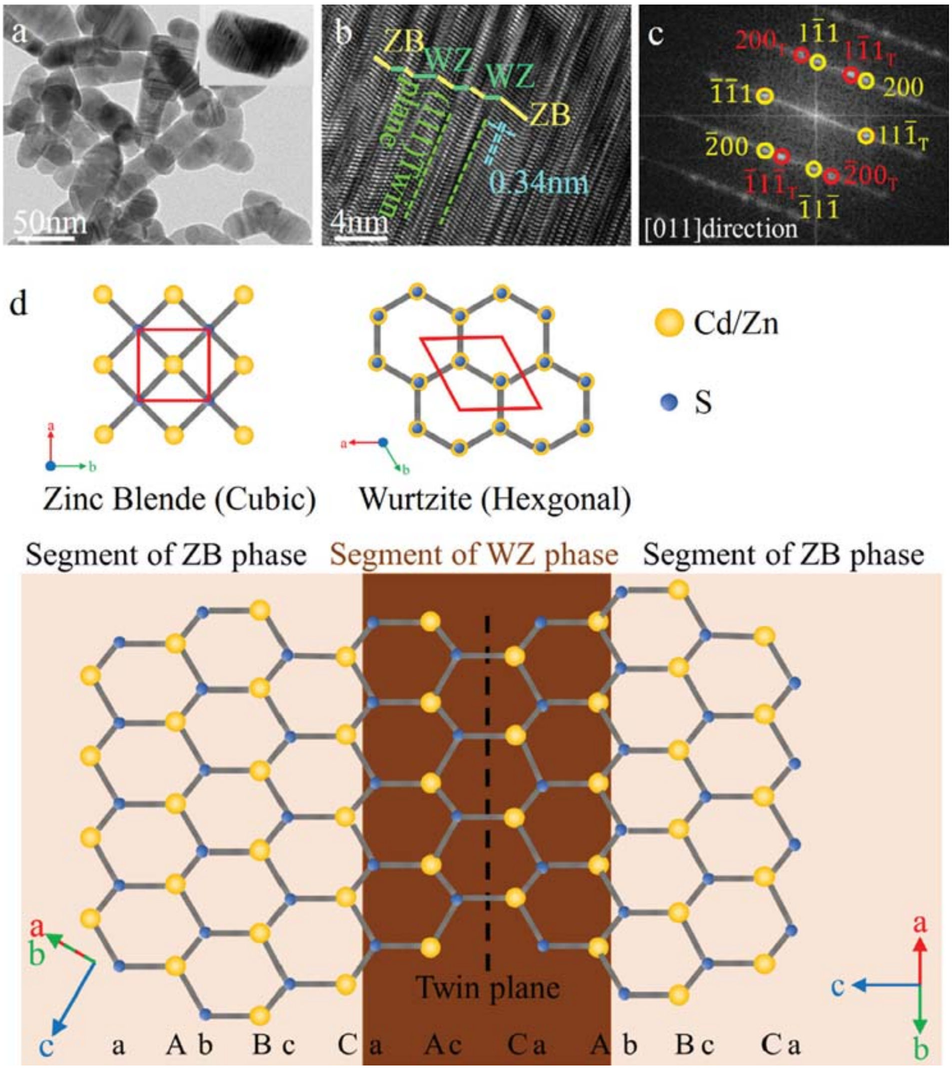

Fig. 2. TEM images of the as-prepared $Cd_{0.6}Zn_{0.4}S$ NCs with high density of twin planes (a), HRTEM of the NC with (1 1 1) twin plane (b), Fast Fourier Transformation (FFT) pattern of a high-resolution (c) and schematic representation of crystal structure of zinc blende and wurtzite phases for $Cd_{1-x}Zn_xS$ and ball-stick structure of a typical twin boundary in a zinc blende (ZB) nanocrystal to form ZB–WZ–ZB homojunction (d).

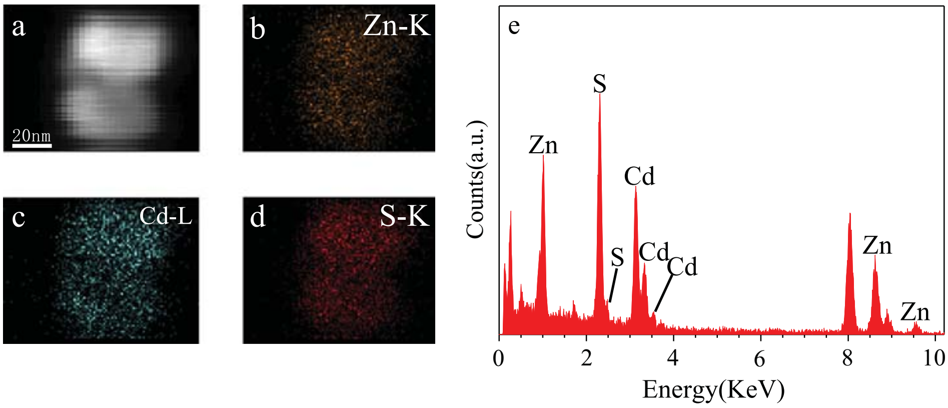

Fig. 3. STEM image (a) of $Cd_{0.6}Zn_{0.4}S$ NCs and the corresponding elemental mapping images (b-d) of the $Cd_{0.6}Zn_{0.4}S$ NCs (e) EDX spectrum of $Cd_{0.6}Zn_{0.4}S$ NCs.

results as mentioned above, the sample can be ascribed to $Cd_{0.6}Zn_{0.4}S$ molecular environments, in agreement with the previously reported values with small variations. In addition, each element's binding energy of all $Cd_{1-x}Zn_xS$ samples was slightly decreased with increasing Zn content (Fig. S4).

3.2. Optical and photoelectrochemical properties

The diffuse reflectance spectra of obtained samples are shown in Fig. 5a. CdS and ZnS have absorption edges determined to be about 530 and 350 nm, respectively, while the absorption edges

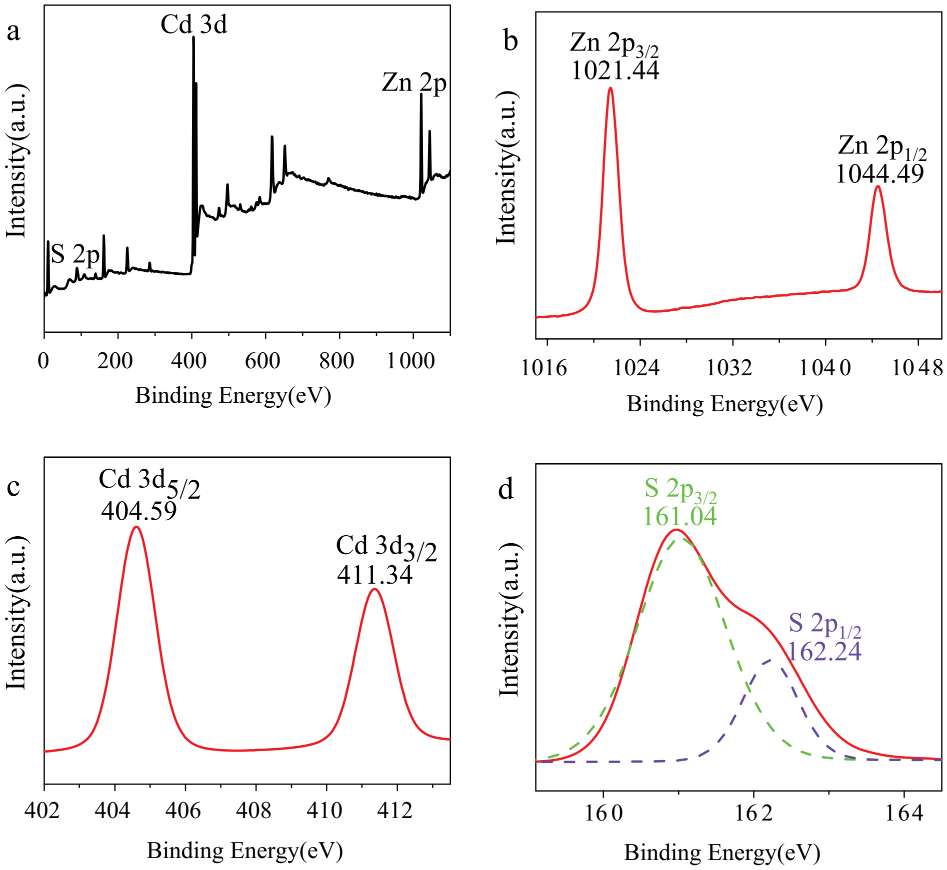

Fig. 4. XPS survey spectrum of $Cd_{0.6}Zn_{0.4}S$ (a) and high-resolution XPS spectra of Zn 2p (b), Cd 3d (c), and S 2p (d).

of $Cd_{1-x}Zn_xS$ solid solutions systematically blue-shift as the Zn^{2+} nominal content is increased, which is attributed to the incorporation of Zn^{2+} into the CdS lattice. A continuous shift of the absorption edges implies that the band gaps of the solid solutions formed between ZnS and CdS can be precisely tuned by varying the Cd/Zn atomic ratios in $Cd_{1-x}Zn_xS$ NCs. The band gaps of $Cd_{1-x}Zn_xS$ photocatalysts can be readily adjusted between 2.28 and 3.50 eV (x = 0–1) (Fig. 5b), as calculated from the onsets of the absorption edges, according to Eq (2) where λ is the wavelength (nm) of the absorption edge [40].

$$E_g = 1240/\lambda \tag{2}$$

The exact values of average band gap energies of as-prepared $Cd_{1-x}Zn_xS$ are presented in Fig. 5c, it is also observed that with the band gap energy increases, color of the samples transforms from yellow to white. Moreover, the valence band (VB) edge position and the conduction band (CB) edge position of the samples are also estimated using the following empirical equation [41,42]:

$$E_{VB} = X - E^e + 1/2E_g \tag{3}$$

$$E_{CB} = E_{VB} - E_g \tag{4}$$

where E_{VB} is the valence band (VB) potential, E_{CB} the conduction band (CB) potential, X the electronegativity of the semiconductor and E^e is the energy of free electrons on the hydrogen scale (about 4.5 eV vs NHE). [43,44]. The computed E_{VB} and E_{CB} of the photocatalysts were also integrated in Fig. 5c.

Photocurrent test (PT) was also performed to detect the photoresponses of $Cd_{1-x}Zn_xS$ NCs. When maintaining identical operational conditions, higher photocurrent intensity implies more efficient electron-hole pairs' separation [45]. As displayed in Fig. 6 and Table S4, when exposed to the light, although all the as-prepared working electrodes of six samples exhibit a quick response, the generated transient photocurrents are different. Under visible light irradiation, the photocurrent density was significantly enhanced with increasing Zn^{2+} content, which can reach a maximum by the optimal sample $Cd_{0.6}Zn_{0.4}S$ (x = 0.4) electrode, whereas further increase of Zn^{2+} content leads to a decrease in the photocurrent density. (see Fig. 7.)

Photoluminescence (PL) spectroscopy has been widely employed to study the photo-generated carriers excitation and the transfer in photocatalysis over semiconductors. Generally speaking, lower PL signals suggest higher photo-induced electron-hole pairs' separation efficiency [46]. Fig. 6b presents the photoluminescence spectra of $Cd_{1-x}Zn_xS$ with different x values under an excitation wavelength of 330 nm. Pure CdS and ZnS displayed higher PL intensity. In contrast, sample $Cd_{0.6}Zn_{0.4}S$ possessed a lower PL signal. The result indicates that the recombination rate of photo-induced electrons and holes pairs was efficiently inhibited, owing to the formation of homojunctions.

3.3. Evaluation of photocatalytic activity

Methylene blue (MB), as a widely used dye, was selected as the model pollutant to evaluate the photoactivity of catalyst. Pure CdS displayed poor photocatalytic activity with only 65% of MB degradation after 80 min irradiation. Simultaneously, for pure ZnS, it could decompose about 58% of MB degradation. As compared to CdS and ZnS, $Cd_{1-x}Zn_xS$ solid solutions showed more superior photocatalytic performance. With the increasing Zn content (x) in the $Cd_{1-x}Zn_xS$ samples, the photoactivity of $Cd_{1-x}Zn_xS$ raised initially, and then when the x value is >0.4, the degradation efficiency of MB

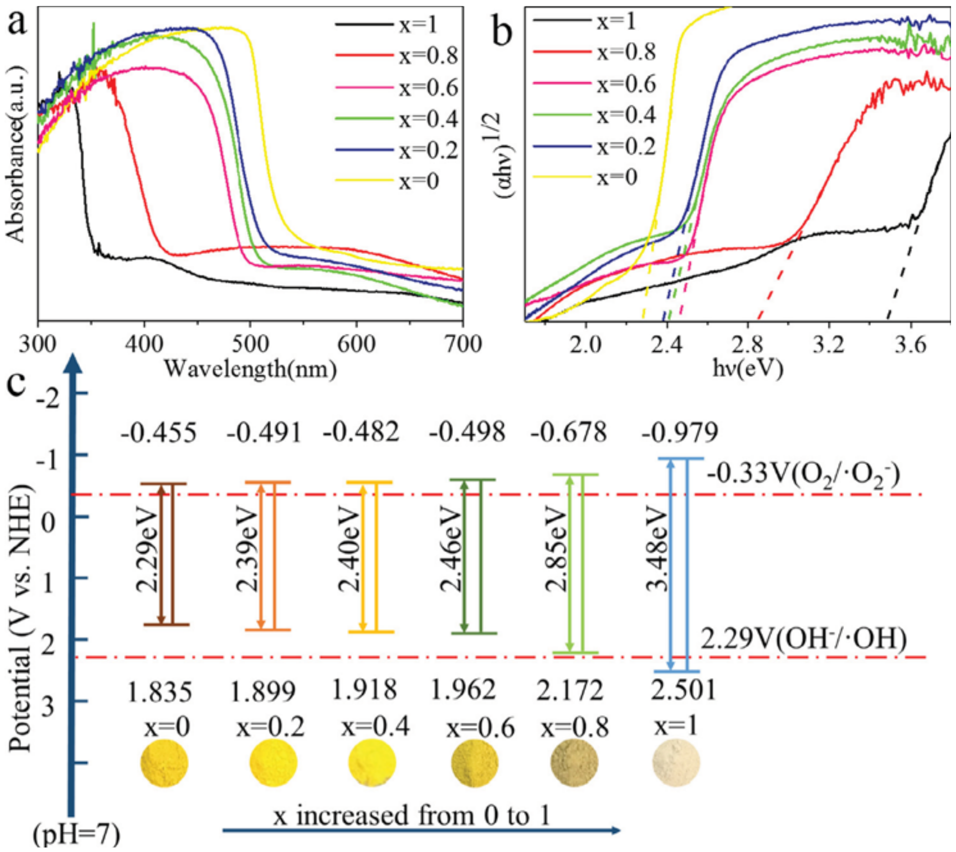

Fig. 5. UV–vis diffuse reflection spectra (a), band gap evaluation from the plots of $(\alpha h\nu)^{1/2}$ vs. the energy of the absorbed light (b), corresponding CB potential, VB potential and band gap energies calculated (c) of $Cd_{1-x}Zn_xS$ samples.

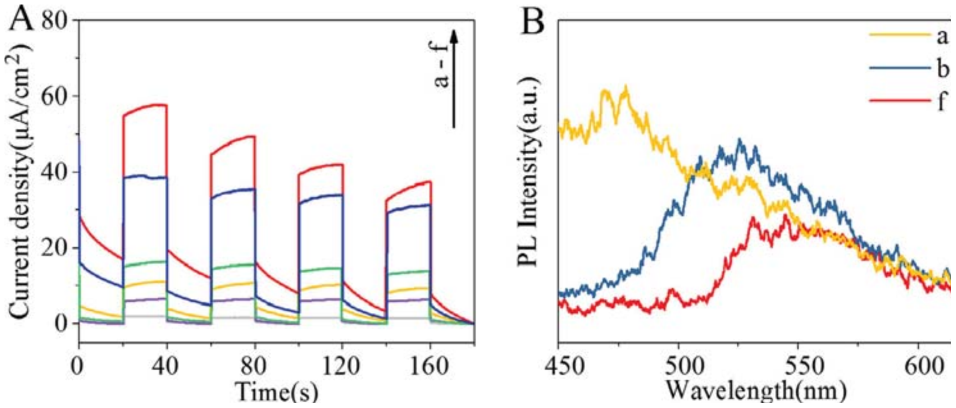

Fig. 6. Photocurrent responses (A), a-f corresponding to x values = 1, 0, 0.8, 0.2, 0.6, 0.4, respectively; and PL spectra (B) of $Cd_{1-x}Zn_xS$, a, b, f corresponding to x values = 1, 0, 0.4, respectively.

begin to fall. The sample of $Cd_{0.6}Zn_{0.4}S$ (x = 0.4) exhibited the highest degradation efficiency (95%) within 80 min of visible-light irradiation.

From the above characterization and experiments, we can infer that photocatalytic performance can't be determined by electric potential of CB and VB directly, it is also dependent on composition, crystal structure and electronic structure. Apart from that the CB and VB have been tuned to adequate electric potential for visible light irradiation redox reaction, the high proportion of long-range ordered twin planes existing in $Cd_{1-x}Zn_xS$ samples is another important factor in photocatalytic performance. For these twin planes can give rise to the generation of myriad homojunctions consisting of alternating zinc-blende (ZB) and wurtzite (WZ) segments along ⟨1 1 1⟩ direction, which were found to be highly efficient in charge separation [17]. Thus, because the carriers' recombination is avoided, the surface radicals relevanting to redox reactions are more easily to generate[47].

3.4. Photostability test

The photostability of $Cd_{0.6}Zn_{0.4}S$ is investigated by recycling the photocatalyst for MB degradation under visible light irradiation (Fig. 8). After each run, the catalyst was collected and washed with deionized water to remove the residual MB, and then put into the

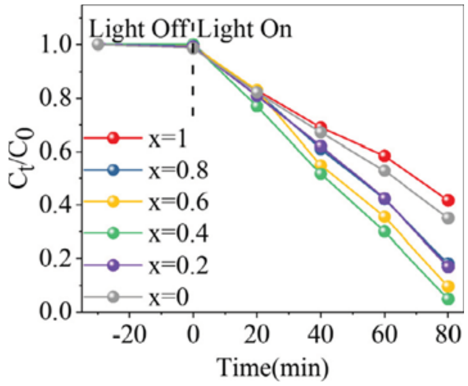

Fig. 7. MB degradation photocatalytic performance of $Cd_{1-x}Zn_xS$ samples under visible light irradiation.

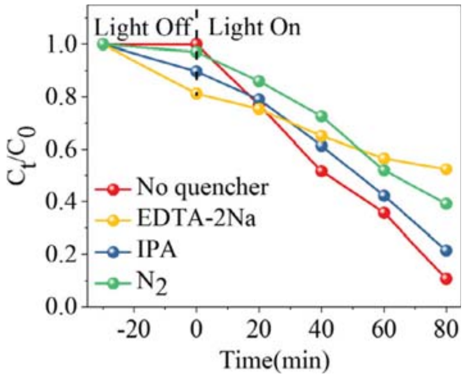

Fig. 9. Effect of different quenchers on the photocatalytic degradation of MB by $Cd_{0.6}Zn_{0.4}S$.

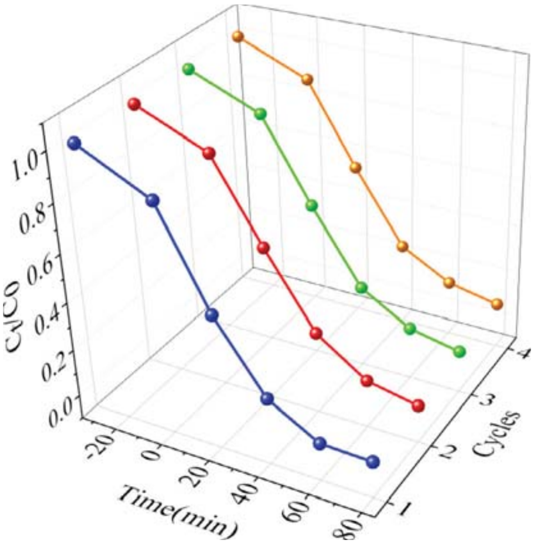

Fig. 8. Cycling test for the photocatalytic degradation of MB (10 mg/L) by $Cd_{0.6}Zn_{0.4}S$.

fresh MB solution to begin a new cycle. During the recycling experiments, all experimental conditions were kept exactly the same with the first cycle experiment. No visible reduction in the decomposition efficiency of MB was found, and the removal rate could still reach 91% in the fourth run (while it was 95% for the first run). This result demonstrate that $Cd_{0.6}Zn_{0.4}S$ was stable in photocatalytic oxidation.

3.5. Photocatalytic degradation mechanism

To clarify the intrinsic mechanism of degradation of MB, the roles of main active species, such as photo-generated holes (h^+), hydroxyl radicals ($^{\cdot}OH$) and superoxide radical ($^{\cdot}O_2^-$) in the photocatalytic process were investigated. In this study, three different quenchers, isopropanol (IPA, $^{\cdot}OH$ scavengers), ethylenediaminetetraacetic acid disodium (EDTA-2Na, h^+ scavengers) and nitrogen (N_2, $^{\cdot}O_2^-$ scavengers) were adopted [44,48,49]. As perceived in Fig. 9, the MB decomposition process was significantly inhibited with EDTA-2Na, implying that holes works in the photocatalytic reaction. Similarly, the addition of N_2 also exhibited a negative effect, indicating that $^{\cdot}O_2^-$ have a significant impact in the reaction system. Relatively, lesser efficiency reduction with the addition of IPA demonstrate that $^{\cdot}OH$ might not be the primary active species. In conclusion, holes, $^{\cdot}O_2^-$ and $^{\cdot}OH$ maybe the main reactive species in the system, while the generation of $^{\cdot}OH$ might come from $^{\cdot}O_2^-$.

The ESR measurements were performed to confirm the reactive oxygen species evolved in the photocatalysis over $Cd_{0.6}Zn_{0.4}S$ NCs with 5,5-dimethyl-1-pyrroline *N*-oxide (DMPO) in aqueous solution. As presented in Fig. 10a, four obvious signals with $Cd_{0.6}Zn_{0.4}S$ in methanol were produced, which could be assigned to DMPO-$^{\cdot}O_2^-$ under light illumination, while no $^{\cdot}O_2^-$ signal was observed in the darkness under identical conditions. The obtained ESR information indicates that O_2 in solution was reduced to generate $^{\cdot}O_2^-$ by photo-generated electrons from $Cd_{0.6}Zn_{0.4}S$ NCs. Similarly, as shown in Fig. 10b, DMPO-$^{\cdot}OH$ signals were also detected in aqueous dispersions of $Cd_{0.6}Zn_{0.4}S$ NCs under visible light illumination time from 4 to 8 min. Both $^{\cdot}O_2^-$ and $^{\cdot}OH$ signals get enhanced as the irradiation time increases.

From the HRTEM image (Fig. 10c) the type-II ZB/WZ heterophase junctions can be clearly identified. Fig. 10d presents the band positions of ZB and WZ phase in $Cd_{0.6}Zn_{0.4}S$ based on experimental results and theoretical calculations [50]. The up-shift of both CB and VB energy levels for WZ segment compared with that of ZB segments could simultaneously lead to efficient separation of both photo-excited electrons and holes. The stimulated electrons were pushed to lower CB energy levels and aggregated on the CB of segments of ZB (away from the twin plane), at the same time, the holes were attracted by higher VB energy levels and aggregated on the VB of segments of WZ (to the twin plane). That is to say, the active sites of oxidation reactions and reduction reactions can be distributed independently and sequentially.

According to the band gap calculation mentioned above, $Cd_{0.6}Zn_{0.4}S$ have an average band gap of about 2.40 eV, the conduction band potential (E_{CB}) of $Cd_{0.6}Zn_{0.4}S$ is about −0.48 V, the value band potential (E_{VB}) of $Cd_{0.6}Zn_{0.4}S$ is about 1.92 V and was more negative than the standard redox potential of $OH^{\cdot}/OH^-$ (2.29 V vs NHE). As a result, the photo-generated electrons on irradiated $Cd_{0.6}Zn_{0.4}S$ can reduce O_2 to give $^{\cdot}O_2^-$, while the photo-generated holes cannot oxidize OH^- to give $^{\cdot}OH$. However, the strong signal peaks of $^{\cdot}OH$ were also observed, it suggests that although the E_{VB} of $Cd_{0.6}Zn_{0.4}S$ limits the photo-generated holes to $^{\cdot}OH$ groups oxidation, the formation of $^{\cdot}OH$ have several ways, the generation of $^{\cdot}OH$ might come from $^{\cdot}O_2^-$, because O_2 or $^{\cdot}O_2^-$ is another source of $^{\cdot}OH$ [51]. The energy of incident light can make the excited electrons from the valence band easily inject into the conduction band. Then O_2 on the surface quickly captures the electrons to yield $^{\cdot}O_2^-$ and H_2O_2. The $^{\cdot}OH$ radical can be formed by the interaction of $^{\cdot}O_2^-$ and H_2O_2.

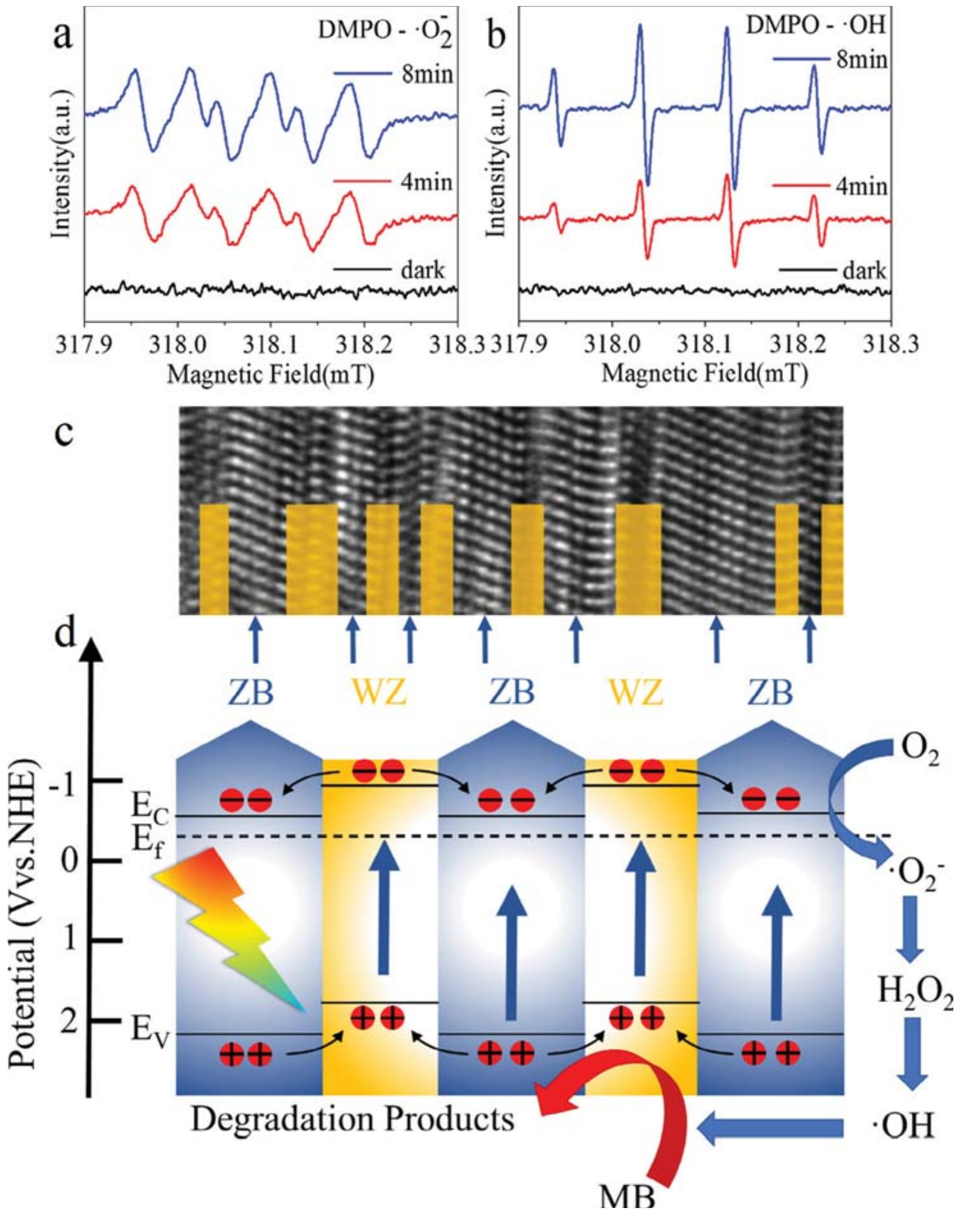

Fig. 10. ESR spectra of radical adducts trapped by DMPO spin-trapping in $Cd_{1-x}Zn_xS$ dispersion in the dark and under visible light irradiation (irradiation time of 4 and 8 min): (a) in methanol dispersion for DMPO-$\cdot O_2^-$; and (b) in aqueous dispersion for DMPO-$\cdot$OH. (c) A schematic illustration of the parallel homojunctions in a real $Cd_{0.6}Zn_{0.4}S$ NC (from TEM image), the blue arrows and yellow squares indicate the segments of ZB and WZ structures, respectively. (d) Mechanism for photo-generated charge separation over the ZB–WZ–ZB homojunction with the type-II staggered band alignment in $Cd_{0.6}Zn_{0.4}S$ photocatalyst. (For interpretation of the references to color in this figure legend, the reader is referred to the web version of this article.)

The above process can be described as follows:

$$Cd_{0.6}Zn_{0.4}S + h\nu \rightarrow e^- + h^+ \quad (5)$$

$$e^- + O_2 \rightarrow \cdot O_2^- \quad (6)$$

$$\cdot O_2^- + H^+ \rightarrow \cdot HO_2 \quad (7)$$

$$2\,\cdot HO_2 \rightarrow H_2O_2 + O_2 \quad (8)$$

$$H_2O_2 + e^- \rightarrow \cdot OH + OH^- \quad (9)$$

$$\cdot OH + MB \rightarrow \text{degradation products} \quad (10)$$

$$h^+ + MB \rightarrow \text{degradation products} \quad (11)$$

4. Conclusions

In this study, we synthesized a series of $Cd_{1-x}Zn_xS$ solid solutions photocatalyst with twin structure by a facile biomolecule-assisted solvothermal route. DRS has demonstrated that the band gaps of the solid solutions are tuneable. The twin structure consisting of coexisting zinc blende and wurtzite phases is the key to homojunctions' formation. The efficient charge separation property has been evaluated by photocurrent tests. Referring band structure calculation, the trapping radicals tests and ESR analysis have demonstrated that $\cdot O_2^-$, $\cdot$OH and h^+ play an important role in degradation process. It is expected that this study can provide a new insight into the strategies for the design and utilization of efficient solar energy-driven photocatalyst for environmental employment.

Acknowledgements

This work was supported by the National Natural Science Foundation of China (51378187, 51478171 and 51672077), Hunan Provincial Natural Science Foundation of China (2017JJ2026).

Appendix A. Supplementary material

Supplementary data associated with this article can be found, in the online version, at https://doi.org/10.1016/j.jcis.2018.02.018.

References

[1] K. Baransi, Y. Dubowski, I. Sabbah, Synergetic effect between photocatalytic degradation and adsorption processes on the removal of phenolic compounds from olive mill wastewater, Water Res. 46 (3) (2012) 789–798.

[2] X. Lin, X. Guo, W. Shi, F. Guo, G. Che, H. Zhai, Y. Yan, Q. Wang, Ag$_3$PO$_4$ quantum dots loaded on the surface of leaf-like InVO$_4$/BiVO$_4$ heterojunction with enhanced photocatalytic activity, Catal. Commun. 71 (2015) 21–27.

[3] X. Lin, S. Yu, Z. Gao, X. Zhang, G. Che, Heterostructured RGO/Bi$_{3.64}$Mo$_{0.36}$O$_{6.55}$ nanospheres: synthesis and enhanced visible-light-driven photocatalytic activity, J. Mol. Catal. A: Chem. 411 (2016) 40–47.

[4] Y. Hong, Y. Jiang, C. Li, W. Fan, X. Yan, M. Yan, W. Shi, In-situ synthesis of direct solid-state Z-scheme V$_2$O$_5$/g-C$_3$N$_4$ heterojunctions with enhanced visible light efficiency in photocatalytic degradation of pollutants, Appl. Catal. B: Environ. 180 (2016) 663–673.

[5] R. Asahi, T. Morikawa, T. Ohwaki, K. Aoki, Y. Taga, Visible-light photocatalysis in nitrogen-doped titanium oxides, Science 293 (5528) (2001) 269–271.

[6] M. Cheng, G. Zeng, D. Huang, L. Cui, P. Xu, C. Zhang, Y. Liu, Hydroxyl radicals based advanced oxidation processes (AOPs) for remediation of soils contaminated with organic compounds: A review, Chem. Eng. J. 284 (2016) 582–598.

[7] X. Li, J. Wen, J. Low, Y. Fang, J. Yu, Design and fabrication of semiconductor photocatalyst for photocatalytic reduction of CO$_2$ to solar fuel, Sci. China Mater. 57 (1) (2014) 70–100.

[8] X. Li, J. Yu, J. Low, Y. Fang, J. Xiao, X. Chen, Engineering heterogeneous semiconductors for solar water splitting, J. Mater. Chem. A 3 (6) (2015) 2485–2534.

[9] M.R. Hoffmann, S.T. Martin, W. Choi, D.W. Bahnemann, Environmental applications of semiconductor photocatalysis, Chem. Rev. 95 (1) (1995) 69–96.

[10] A. Kudo, Y. Miseki, Heterogeneous photocatalyst materials for water splitting, Chem. Soc. Rev. 38 (1) (2009) 253–278.

[11] X. Chen, S. Shen, L. Guo, S.S. Mao, Semiconductor-based photocatalytic hydrogen generation, Chem. Rev. 110 (11) (2010) 6503–6570.

[12] X. Lang, X. Chen, J. Zhao, Heterogeneous visible light photocatalysis for selective organic transformations, Chem. Soc. Rev. 43 (1) (2014) 473–486.

[13] A.J. Bard, M.A. Fox, Artificial photosynthesis: solar splitting of water to hydrogen and oxygen, Accounts Chem. Res. 28 (3) (1995) 141–145.

[14] J. Wen, X. Li, W. Liu, Y. Fang, J. Xie, Y. Xu, Photocatalysis fundamentals and surface modification of TiO$_2$ nanomaterials, Chinese J. Catal. 36 (12) (2015) 2049–2070.

[15] A.J. Bard, Photoelectrochemistry, Science 207 (4427) (1980) 139–144.

[16] A.L. Linsebigler, G. Lu, J.T. Yates Jr, Photocatalysis on TiO$_2$ surfaces: principles, mechanisms, and selected results, Chem. Rev. 95 (3) (1995) 735–758.

[17] M. Liu, D. Jing, Z. Zhou, L. Guo, Twin-induced one-dimensional homojunctions yield high quantum efficiency for solar hydrogen generation, Nat. Commun. 4 (2013) 2278.

[18] M. Liu, Y. Du, L. Ma, D. Jing, L. Guo, Manganese doped cadmium sulfide nanocrystal for hydrogen production from water under visible light, Int. J. Hydrogen Energy 37 (1) (2012) 730–736.

[19] H. Tada, T. Mitsui, T. Kiyonaga, T. Akita, K. Tanaka, All-solid-state Z-scheme in CdS-Au-TiO$_2$ three-component nanojunction system, Nat. Mater. 5 (10) (2006) 782–786.

[20] H. Yan, J. Yang, G. Ma, G. Wu, X. Zong, Z. Lei, J. Shi, C. Li, Visible-light-driven hydrogen production with extremely high quantum efficiency on Pt–PdS/CdS photocatalyst, J. Catal. 266 (2) (2009) 165–168.

[21] M.T. Mayer, Y. Lin, G. Yuan, D. Wang, Forming heterojunctions at the nanoscale for improved photoelectrochemical water splitting by semiconductor materials: case studies on hematite, Acc. Chem. Res. 46 (7) (2013) 1558–1566.

[22] X. Wang, Q. Xu, M. Li, S. Shen, X. Wang, Y. Wang, Z. Feng, J. Shi, H. Han, C. Li, Photocatalytic overall water splitting promoted by an alpha-beta phase junction on Ga$_2$O$_3$, Angew.Chem. Int. Ed. Engl. 51 (52) (2012) 13089–13092.

[23] X. Zong, H. Yan, G. Wu, G. Ma, F. Wen, L. Wang, C. Li, Enhancement of photocatalytic H$_2$ evolution on CdS by loading MoS$_2$ as cocatalyst under visible light irradiation, J. Am. Chem. Soc. 130 (23) (2008) 7176–7177.

[24] M. Liu, L. Wang, G. Lu, X. Yao, L. Guo, Twins in Cd$_{1-x}$Zn$_x$S solid solution: Highly efficient photocatalyst for hydrogen generation from water, Energy Environ. Sci. 4 (4) (2011) 1372.

[25] W. Li, D. Li, W. Zhang, Y. Hu, Y. He, X. Fu, Microwave synthesis of ZnxCd1− xS nanorods and their photocatalytic activity under visible light, 2010.

[26] K.-I. Ishibashi, A. Fujishima, T. Watanabe, K. Hashimoto, Detection of active oxidative species in TiO$_2$ photocatalysis using the fluorescence technique, Electrochem. Commun. 2 (3) (2000) 207–210.

[27] M. Kruk, M. Jaroniec, Gas adsorption characterization of ordered organic-inorganic nanocomposite materials, Chem. Mater. 13 (10) (2001) 3169–3183.

[28] K. Sing, Reporting physisorption data for gas/solid systems with special reference to the determination of surface area and porosity (Provisional), Pure Appl. Chem. 54 (11) (1982) 2201–2218.

[29] D. Everett, R. Haul, L. Moscou, R. Pierotti, J. Rouquerol, T. Siemieniewska, Reporting physisorption data for gas solid systems with special reference to the determination of surface-area and porosity (recommendations 1984), Pure Appl. Chem. 57 (1985) 603.

[30] J. Yu, L. Qi, M. Jaroniec, Hydrogen production by photocatalytic water splitting over Pt/TiO$_2$ nanosheets with exposed (001) facets, J. Phys. Chem. C 114 (30) (2010) 13118–13125.

[31] M. Chen, E. Ma, K.J. Hemker, H. Sheng, Y. Wang, X. Cheng, Deformation twinning in nanocrystalline aluminum, Science 300 (5623) (2003) 1275–1277.

[32] S. LuL, Ultra high strength and high electrical conductivity in copper, Science 304 (5669) (2004) 422–426.

[33] L. Yonghong, W. Pingxiao, H. Junyi, T. Lytuong, Z. Nengwu, D. Zhi, Alkaline-assisted hydrothermal fabrication of CdZnS with enhanced visible-light photocatalytic performance, Chem. J. Chinese Univ.-Chinese 36 (8) (2015) 1563–1569.

[34] Q. Li, X. Gong, C. Wang, J. Wang, K. Ip, S. Hark, Size-dependent periodically twinned ZnSe nanowires, Adv. Mater. 16 (16) (2004) 1436–1440.

[35] Y. Yan, R. Noufi, M.M. Al-Jassim, Grain-boundary physics in polycrystalline CuInSe$_2$ revisited: experiment and theory, Phys. Rev. Lett. 96 (20) (2006) 205501.

[36] K. Maeda, A. Xiong, T. Yoshinaga, T. Ikeda, N. Sakamoto, T. Hisatomi, M. Takashima, D. Lu, M. Kanehara, T. Setoyama, T. Teranishi, K. Domen, Photocatalytic overall water splitting promoted by two different cocatalysts for hydrogen and oxygen evolution under visible light, Angew. Chem. Int. Ed. Engl. 49 (24) (2010) 4096–4099.

[37] L. Wang, Z. Yao, F. Jia, B. Chen, Z. Jiang, A facile synthesis of Zn$_x$Cd$_{1-x}$S/CNTs nanocomposite photocatalyst for H$_2$ production, Dalton Trans. 42 (27) (2013) 9976–9981.

[38] S.N. Guo, Y.L. Min, J.C. Fan, Q.J. Xu, Stabilizing and improving solar H$_2$ Generation from Zn$_{0.5}$Cd$_{0.5}$S Nanorods@MoS$_2$/RGO hybrids via dual charge transfer pathway, ACS Appl. Mater. Interfaces 8 (5) (2016) 2928–2934.

[39] S. Zhao, J. Huang, Q. Huo, X. Zhou, W. Tu, A non-noble metal MoS2-Cd0.5Zn0.5S photocatalyst with efficient activity for high H2evolution under visible light irradiation, J. Mater. Chem. A 4 (1) (2016) 193–199.

[40] Y. Zang, L. Li, X. Li, R. Lin, G. Li, Synergistic collaboration of g-C$_3$N$_4$/SnO$_2$ composites for enhanced visible-light photocatalytic activity, Chem. Eng. J. 246 (2014) 277–286.

[41] K. Katsumata, R. Motoyoshi, N. Matsushita, K. Okada, Preparation of graphitic carbon nitride g-C$_3$N$_4$/WO$_3$ composites and enhanced visible-light-driven photodegradation of acetaldehyde gas, J. Hazard. Mater. 260 (2013) 475–482.

[42] C. Zhou, C. Lai, D. Huang, G. Zeng, C. Zhang, M. Cheng, L. Hu, J. Wan, W. Xiong, M. Wen, Highly porous carbon nitride by supramolecular preassembly of monomers for photocatalytic removal of sulfamethazine under visible light driven, Appl. Catal. B Environ. 220 (2017).

[43] H. Li, J. Liu, W. Hou, N. Du, R. Zhang, X. Tao, Synthesis and characterization of g-C$_3$N$_4$/Bi$_2$MoO$_6$ heterojunctions with enhanced visible light photocatalytic activity, Appl. Catal. B: Environ. 160–161 (2014) 89–97.

[44] H. Wang, X. Yuan, H. Wang, X. Chen, Z. Wu, L. Jiang, W. Xiong, G. Zeng, Facile synthesis of Sb$_2$S$_3$/ultrathin g-C$_3$N$_4$ sheets heterostructures embedded with g-C$_3$N$_4$ quantum dots with enhanced NIR-light photocatalytic performance, Appl. Catal. B: Environ. 193 (2016) 36–46.

[45] H. Li, Y. Sun, B. Cai, S. Gan, D. Han, L. Niu, T. Wu, Hierarchically Z-scheme photocatalyst of Ag@AgCl decorated on BiVO$_4$ (040) with enhancing photoelectrochemical and photocatalytic performance, Appl. Catal. B: Environ. 170–171 (2015) 206–214.

[46] Z. Zhang, D. Jiang, D. Li, M. He, M. Chen, Construction of SnNb$_2$O$_6$ nanosheet/g-C$_3$N$_4$ nanosheet two-dimensional heterostructures with improved photocatalytic activity: synergistic effect and mechanism insight, Appl. Catal. B: Environ. 183 (2016) 113–123.

[47] S. Bai, J. Jiang, Q. Zhang, Y. Xiong, Steering charge kinetics in photocatalysis: intersection of materials syntheses, characterization techniques and theoretical simulations, Chem. Soc. Rev. 44 (10) (2015) 2893–2939.

[48] F. Chen, Q. Yang, J. Sun, F. Yao, S. Wang, Y. Wang, X. Wang, X. Li, C. Niu, D. Wang, G. Zeng, Enhanced photocatalytic degradation of tetracycline by AgI/BiVO$_4$ heterojunction under visible-light irradiation: mineralization efficiency and mechanism, ACS Appl. Mater. Interfaces 8 (48) (2016) 32887–32900.

[49] T. Cai, Y. Liu, L. Wang, S. Zhang, Y. Zeng, J. Yuan, J. Ma, W. Dong, C. Liu, S. Luo, Silver phosphate-based Z-Scheme photocatalytic system with superior sunlight photocatalytic activities and anti-photocorrosion performance, Appl. Catal. B Environ. 208 (2017) 1–13.

[50] J. Shi, H.n. Cui, Z. Liang, X. Lu, Y. Tong, C. Su, H. Liu, The roles of defect states in photoelectric and photocatalytic processes for Zn$_x$Cd$_{1-x}$S, Energy Environ. Sci. 4 (2) (2011) 466–470.

[51] P. Salvador, On the nature of photogenerated radical species active in the oxidative degradation of dissolved pollutants with TiO$_2$ aqueous suspensions: a revision in the light of the electronic structure of adsorbed water, J. Phys. Chem. C 111 (45) (2007) 17038–17043.